Design of Surface Plasmon Resonance Sensor Based on A Triple-Layer Silicon Waveguide

Yu-Cheng Lin*

Department of Electronic Engineering, Ming Chuan University

ABSTRACT

This article presents a theoretical investigation into the design of a surface plasmon resonance (SPR) sensor based on a triple-layer silicon waveguide. The sensor incorporates an optical waveguide with a deposited thin-film layer of silver, forming a three-layer structure on a silicon substrate with buried oxide. The discussion centers around the excitation conditions of SPR and the selection of waveguide material, considering dispersion characteristics and the effective refractive index perspective. Addressing the design considerations for SPR sensor dimensions, we propose adopting a waveguide thickness of 0.22 µm compatible with CMOS processes. Further calculations reveal the optimal range for silver film thickness to be between 20 nm and 60 nm, with a recommended sensing length exceeding 25 µm. Employing these optimized parameters, we derive a sensitivity function correlated with the refractive index of the analyte, achieving a theoretical maximum sensitivity of up to 7.956 µm/RIU.

Keywords: surface plasmon resonance, silicon photonics, effective refractive index, sensitivity

基於三層矽波導的表面電漿共振感測器設計

林鈺城*

銘傳大學電子工程學系

摘 要

本研究理論上探討了一種基於三層矽波導的表面電漿共振 (Surface Plasmon Resonance)感測器的設計。感測器利用光波導上覆蓋了一層沉積的銀薄膜,加上待測物後,構成三層結構,並置於有氧化埋層的矽基板上。基於材料的色散特性,以有效折射率的觀點,論述了 SPR 的激發條件與波導材料的選擇。波導採用與 CMOS 製程兼容的厚度 $0.22~\mu$ m,針對 SPR 元件尺寸的設計考量,我們計算出銀薄膜厚度較佳範圍為 $20~\mathrm{nm}$ 至 $60~\mathrm{nm}$,並且感測長度要超過 $25~\mu$ m。根據提出的優化參數,分析了 SPR 感測器的靈敏度,得到靈敏度與待測物折射率的相關函數,並可計算出靈敏度最高可達 $7.956~\mu$ m/RIU。

關鍵詞:表面電漿共振,矽光子,有效折射率,靈敏度

文稿收件日期 113.01.24;文稿修正後接受日期 113.11.18; *通訊作者 Manuscript received Jan 24, 2024; revised Nov 18, 2024; * Corresponding author

I. INTRODUCTION

Silicon photonics is a technology that involves the integration of photonic or optical functions, such as the generation, manipulation, and detection of light, on a silicon-based integrated circuit (IC) chip. This approach enables cost-effective and high-volume manufacturing. In the realm of building photonic integrated circuits (PIC), various technology including III-V platforms coexist, semiconductors, Lithium Niobate, high-index nitrides, polymers, and glasses, notably, silicon[1]. What distinguishes silicon photonics is its seamless alignment with the manufacturing and tools employed processes metal-oxide-semiconductor complementary (CMOS) industry. This alignment opens the door to large-scale production with the potential for reduced per-device costs [2].

Surface plasmon resonance (SPR) has emerged as a remarkably versatile and valuable sensing tool among the various optical sensors, presenting significant research prospects and widespread commercial applications [3-7]. Fundamentally, the phenomenon of surface plasmon resonance (SPR) relies on the displacement of resonant peaks within the SPR spectrum caused by changes in the dielectric constant of the surrounding environment near the sensing region. Employing the Kretschmann configuration [8], SPR-based sensors have gained recognition notable for their versatile applicability in diverse sensing scenarios. Recently, the design and fabrication of novel SPR sensor platforms have garnered substantial attention. Researchers have explored diverse strategies to enhance sensor sensitivity. selectivity, and versatility. This has led to the development of specialized sensor configurations, such as prism-based SPR sensors [9, 10], waveguide-based SPR sensors [11-13], optical fiber-based SPR sensors [14-16] and plasmonic nanostructures [7, 17], each tailored to specific analytical needs. Especially, the evolution of SPR technology in biosensors has yielded notable advantages. Its label-free nature, real-time monitoring capabilities, and high sensitivity make SPR a powerful tool for studying biomolecular interactions [5, 7, 18, 19]. This technology enables rapid and accurate analysis of binding kinetics, affinities, and concentrations, thus facilitating enhanced understanding in fields

like drug discovery, medical diagnostics, and molecular biology.

During this period, silicon-based PICs were initially established for telecommunications and later extensively developed for biosensing applications over 15 years ago [20, 21]. Both SPR and PIC technologies offer the benefit of labelfree, real-time molecule detection. Additionally, they enable the simultaneous detection of multiple analytes within a single sample through multiplexing. In SPR, this is achieved by partitioning the sensor surface into distinct sensing spots. While, in PIC, multiplexing is seamlessly achieved by producing multiple sensors on a single chip. In both instances, the preferred approach for generating extensive sensor arrays is currently through spotting technology.

For the development of sensors, theoretical design and simulation form the fundamental stages. One fundamental point in the design of SPR sensors is to fine-tune the conditions for the existence of coupling between the excitation field and the Surface Plasmon Polariton (SPP) that propagates at the interface of the metal and the sample medium. To enhance this crucial aspect, a wide array of diverse structural configurations has been introduced in recent times, primarily centered around various approaches to generate SPP and sensor interrogation techniques. These innovations have facilitated the creation of highly sensitive sensors, including compact structures reliant on optical waveguides [22]. However, there remains a pressing need for cost-effective solutions that can enhance healthcare accessibility and the diagnosis of infectious and chronic diseases [23]. There is considerable interest in developing novel strategies to extend the exceptional detection capabilities of SPR sensors to the realm of affordable materials and devices [24].

To fabricate sensors on silicon wafers, there are two main options for waveguide materials, silicon and silicon dioxide, i.e. silica. Silicon waveguides are widely used in integrated photonics due to their compatibility with CMOS fabrication processes and their ability to confine and manipulate light on a chip [25]. Regarding its optical properties, silicon exhibits transparency within the wavelength range of 1.1 to 8 μm, encompassing the near-infrared (NIR) and certain segments of the mid-infrared (MIR) region[25, 26]. Silicon has a high refractive index (RI) contrast with its oxide layer (silica, SiO₂),

enabling strong light confinement and compact device sizes. Silicon waveguides can achieve low propagation losses, especially telecommunication wavelength range. However, silicon has a relatively high coefficient of thermal expansion, which can lead to thermal shifts in the wavelength, affecting operating performance[25]. Efficiently coupling light into and out of silicon waveguides can be challenging due to the mode mismatch with standard optical fibers [26]. Owing to the high RI of silicon (3.45), it is hard to apply as an optical or sensing medium, especially the SPR sensors[27, 28] and lossy mode resonance sensors[29, 30].

Silica waveguides are widely used in photonics and integrated optics due to their low compatibility with microfabrication techniques [26]. Silica proves to be a compelling material for passive PICs owing to its well-established fabrication process, minimal propagation loss, and compatibility with optical silica fibers. Moreover, silica materials demonstrate low absorption across the visible to the MIR spectrum. They are used in various including telecommunications, applications, sensors, and lasers. There are two common fabrication methods for silica waveguides. The first one is the Ion exchange method [31, 32]. This involves replacing ions in a glass substrate with larger ions from a molten salt bath. This change in ion size creates an RI change, forming a waveguide. The ion exchange process can be relatively simple and cost-effective. Moreover, waveguides produced through exchange often exhibit low optical losses, particularly in comparison to some other fabrication methods. However, the RI change achievable through ion exchange may be limited, which can impact the effectiveness of waveguide devices that rely on strong index contrasts, such as Mach-Zehnder interferometers or photonic crystal structures. The other method is Plasma Enhanced Chemical Vapor Deposition (PECVD) [33, 34]. PECVD is used to deposit thin films of silica onto substrates.

By adjusting the SiH/N₂O flow ratio in the PECVD process, the structure of the deposited SiO₂ layer can be modified to form SiOx. This alteration influences the RI of the deposited layer, with the RI being proportional to the SiH/N₂O flow ratio. Utilizing this technology allows for a flexible waveguide design, enabling the variation of RI contrast from 5 x 10⁻³ to 0.5. Consequently, the waveguide design can be tailored to meet

diverse requirements for the RI and optical field profiles. Therefore, the waveguide design utilizes the PECVD process to ensure that the RI of the waveguide is about 0.004 higher than that of the silica substrate [33]. This also introduces an additional design parameter for the SPR sensor.

This paper presents a comprehensive overview of SPR and PIC technologies. Through this comparative analysis with the well-established SPR, we aim to enhance the understanding of the innovative PIC technology.

According to the SPR theory and dispersion model, the suitability of silicon and silica as SPR waveguide materials is compared. Following the simulation results, the discussion will focus on the primary dimensional parameters for designing the SPR sensor and propose design principles. Furthermore, based on the optimized design parameters of the SPR sensor, sensitivity will be derived as a function of the analyte's refractive index, and comparisons will be made with results from the literature.

II. THEORY

Surface plasmons, or surface plasma waves, represent electromagnetic modes that arise at the interface between a metal and a dielectric medium. When a metal thin film is deposited onto a glass substrate and comes into contact with a dielectric material, it supports oscillations in charge density [35]. Within a conductor, a multitude of negatively charged free electrons exists, typically on the order of 10²³ electrons per cubic centimeter. These free electrons coexist with a lattice of positively charged ions, but due to the immense mass of the ions compared to the electrons, the ions can effectively be replaced by a constant positive background charge. Despite this, the total charge density inside the conductor remains neutral. However, when an external field is applied to perturb the density of free electrons, they begin to move in response. They are drawn toward the positive ion background, creating an attractive driving force. This movement leads to an accumulation of electrons over what is needed for charge neutrality. The surplus of electrons results in Coulomb repulsion, acting as a restoring force that initiates motion in the opposite direction. The interplay between these forces—attraction and repulsion—causes longitudinal oscillations in the free electrons, known as plasma oscillations.

2.1 Resonance conditions

Direct excitation of surface plasmons over a metal-dielectric interface by incident light is challenging because the wave numbers of surface plasmons are typically greater than those of the incident light in the dielectric waveguide. The wave numbers depend on three factors, namely the RI of the medium, the wavelength of the incident light, and the incident angle. For the convenience of illustration, the wavelength and RI are fixed, and only the incident angle is concerned. To induce SPR, specific geometries are employed, and p-polarized light is utilized. When p-polarized light strikes the interface between the waveguide and metal, and the incident angle falls within a certain range, total internal reflection occurs. Resonance occurs when the wave vector of the incident light aligns with the oscillation frequency of electrons at the surface of the metal film. This alignment results in the absorption of light energy and a decrease in the intensity of reflected light, causing a dip in the reflected light intensity at a specific incident angle. Referred to as the resonance angle of SPR, this angle varies depending on the RI combinations of the metal and dielectric materials.

SPR is a resonance phenomenon formed by the evanescent wave passing through the waveguide to excite the metal surface plasmon wave (SPW), which satisfies the Maxwell equations and the continuous relationship. Upon incorporating the boundary conditions, we can calculate the wave vector, denoted as k_{sp} , for the surface plasma wave. It can be determined using eq. (1), where ε_m represents the dielectric constant of the metal, ε_d represents the dielectric constant of the analyte above it, λ stands for the wavelength, and k_0 is the wave vector in a vacuum ($k_0=2\pi/\lambda$). This formula shows that the wave vector of the surface plasma wave is determined by the material of the metal and the upper analyte.

$$k_{sp} = k_0 \left(\frac{\varepsilon_m \varepsilon_d}{\varepsilon_m + \varepsilon_d} \right)^{\frac{1}{2}} \tag{1}$$

On the other hand, the evanescent wave $k_{\rm ev}$ at a specific incident angle θ_{sp} is shown in Eq. (2). Resonance is achieved when the wave vector of the SPW aligns with the evanescent wave vector, which represented as $k_{\rm ev} = k_{sp}$.

$$k_{\rm ev} = k_0 n_p \sin \theta_{sp} \tag{2}$$

The wave vector of SPW (k_{sp}) is a complex number. The successful excitation of SPW depends on the presence of a positive real component in k_{sp} . This essential condition is satisfied by a wide range of metal-dielectric combinations across spectra. The propagation length of the SPW is determined by the imaginary part of k_{sp} . When the imaginary part of k_{sp} becomes significantly large, it makes practical applications of the SPW impractical.

2.2 Material dispersion

Material dispersion refers to the phenomenon where the speed of light in a material varies with its frequency. This variation can lead to the spreading out of different wavelengths of light as they propagate through the material. This dispersion effect is a result of the interaction between light and the material's atomic or molecular structure, which can lead to changes in the material's RI at different wavelengths. This dispersion is closely related to the complex nature of the RI of a material, which includes both a real part (related to the speed of light) and an imaginary part (related to absorption). Both real and imaginary parts of the RI contribute to the overall behavior of material dispersion. The dielectric constant and RI are closely related parameters that describe how a material interacts with electromagnetic waves. Material dispersion has important implications in telecommunications. Managing optics material dispersion is crucial in the design and optimization of optical devices to ensure accurate and efficient light propagation and signal transmission. The dispersion analysis of the materials to be utilized in this design is as follows. The dispersion data for silicon was sourced from [36]. Subsequently, a curve-fitting methodology will be applied to determine the expressions for the dispersion curves, specifically represented as eq.3(a) and eq.3(b). Here, n_{Si} and k_{Si} respectively denote the real RI and the imaginary RI of silicon.

$$n_{Si}(\lambda) = 3.697 + 98.245 \cdot e^{-10.166 \cdot \lambda}$$
 (3a)

$$k_{Si}(\lambda) = 0.011 + 253.04 \cdot e^{-16.725 \cdot \lambda}$$
 (3b)

The dielectric constant of silica varies with wavelength according to Sellmeire dispersion relation as eq. (4) where λ is the wavelength in

 μ m and a_1 , a_2 , a_3 , b_1 , b_2 and b_3 are Sellmeier coefficients [37].

$$\varepsilon_{silica}(\lambda) = 1 + \frac{a_1 \lambda^2}{\lambda^2 - b_1^2} + \frac{a_2 \lambda^2}{\lambda^2 - b_2^2} + \frac{a_3 \lambda^2}{\lambda^2 - b_3^2}$$
 (4)

Simulation necessitates the inclusion of the dielectric function of the metallic layer. According to the Drude formula, the dielectric function of any metal (ε_m) can be expressed as eq. (5).

$$\varepsilon_{\rm m}(\lambda) = 1 - \frac{\lambda_{\rm c} \lambda^2}{\lambda_{\rm p}^2 (\lambda_{\rm c} + i\lambda)}$$
 (5)

where λ_p and λ_c represent the plasma and the collision wavelengths, respectively [38].

2.3. Normalized transmitted power

For generality, Fig. 1 illustrates a three-layer configuration comprising a planar waveguide with a thickness denoted as d_1 and a RI of n_1 , a metal layer with a thickness of d_2 and a complex RI represented as $n_2 + .jk_2$, and a covering layer composed of the analyte with an RI of n_3 . This three-layer structure is constructed on a silicon substrate with buried oxide (BOX) and its sufficient thickness serves to block the influence of the high RI silicon substrate below on the coupling effect.

The collimated source is introduced into one end of the optical waveguide. The power (P) reaching the end of the waveguide at the incident angle (θ) , is expressed by equation (6). [37]

$$P(\theta) = \frac{n_1^2 sin\theta cos\theta}{(1 - n_1^2 cos^2\theta)^2} \tag{6}$$

Since SPR only occurs in the p-polarized mode, s-polarized light will be omitted in the subsequent discussion. Using the reflectance at the waveguide and metal interface, the normalized transmitted power (P_{trans}) of p-polarized light is as eq. (7).

$$P_{trans} = \frac{\int_{\theta_{cr}}^{\pi/2} R_p^{N_{ref}(\theta)} P(\theta) d\theta}{\int_{\theta_{cr}}^{\pi/2} P(\theta) d\theta}$$
 (7)

The notation $N_{ref}(\theta)$ represents the overall count of light reflections undergone by a ray at an angle θ relative to the interface's normal in the sensing region. It is defined as $L/(2D \cdot \tan \theta)$. Here, L represents the length of the exposed sensing region, and D is the thickness of the

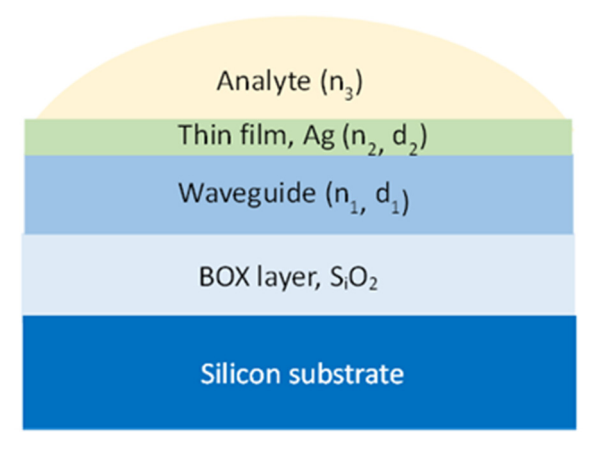


Fig.1. Three-layer sensing structure deposited on a silicon substrate with the BOX layer

waveguide. θ_{cr} is the critical angle of the waveguide. The reflectance R_p can be derived from the optical reflection matrix of the multilayer film. One can assess the reflection coefficient of the multi-layered structure by using the transfer matrix approach for the N-layer model [39]. In the current investigation, three layers exist on the BOX layer, giving rise to three interfaces. The thickness and dielectric constant of the arbitrary (kth) medium layer are represented as d_k and ε_k , respectively. In the N-layer model, the relationship between the tangential field components at the first and last interfaces is expressed in eq. (8).

$$\begin{bmatrix} E_1 \\ H_1 \end{bmatrix} = M \begin{bmatrix} E_{N-1} \\ H_{N-1} \end{bmatrix} \tag{8}$$

 E_1 and H_1 denote the electric and magnetic fields at the first interface, while E_{N-1} and H_{N-1} represent those at the (N-1)th interface. Additionally, M is referred to as the N-layer matrix, and its expression is provided in eq. (9).

$$M = \prod_{k=2}^{N-1} M_k = \begin{bmatrix} M_{11} & M_{12} \\ M_{21} & M_{22} \end{bmatrix}$$
 (9)

where M_k is written as eq. (10).

$$M_{K} = \begin{bmatrix} \cos \beta_{K} & -i \sin \beta_{k} / q_{k} \\ -i q_{k} \sin \beta_{k} & \cos \beta_{k} \end{bmatrix} \quad (10)$$

 q_k and β_k are given as $q_k = \sqrt{\varepsilon_k - n_1^2 \sin^2 \theta}$ and $\beta_k = 2\pi d_k q_k / \lambda$. The reflection coefficient (r_p) is as eq. (11)

$$r_p = \frac{(M_{11} + M_{12}q_4)q_1 - (M_{21} - M_{22}q_4)}{(M_{11} + M_{12}q_4)q_1 + (M_{21} - M_{22}q_4)}$$
(11)

Moreover, the reflectance R_p of a p-polarized light is presented as eq. (12)

$$R_p = |r_p|^2 \tag{12}$$

III. RESULTS

To facilitate a more focused discussion on SPR sensors, simulations for material dispersions and component dimensions will be conducted using the most commonly employed materials: silicon, silica, and silver.

3.1 Dispersion

According to the wavelength from 0.4 μm to 1.8 μm, the simulation results of the dispersion curves of the three materials are shown in Fig 2. In the visible and near-infrared spectral range, the real part of the RI of silicon exhibits typical dispersion (solid blue line). This indicates that at shorter wavelengths, the RI is higher, with a value of 5.383 at a wavelength of 0.4 μm, compared to longer wavelengths where it is 3.702 at a wavelength of 1.8 μm. This is a common dispersion behavior in most transparent materials. The imaginal part of the RI of silicon (dotted blue line) is closely related to the x-axis. This implies very low absorption in the wavelength range.

The RI variation of silica also decreases with the increasing wavelength, ranging from 1.471 to 1.443. The dispersion variation is relatively less pronounced compared to silicon. The dispersion curve of silver exhibits distinct characteristics. As the wavelength increases, there is a substantial increase in the real part of the RI, causing a shift from lower to higher values. However, it's important to note that in the visible and nearinfrared range, the real part of the RI remains relatively low from 0.033 to 0.630. Additionally, the imaginary part of the RI for silver experiences a significant increase from 2.562 to 12.290. This suggests a strong absorption of light, particularly in the near-infrared wavelength regions. The interplay between the real and imaginary parts of the RI contributes to the material's plasmonic properties, making silver important component in various applications involving SPR and other related phenomena.

3.2 Waveguide material for SPR

From the resonance condition in eq.(1) and

eq.(2), the effective RI (n_{eff}) as SPR occurs can be defined as eq.(13).

$$n_{eff} = \sqrt{\frac{\varepsilon_2 \varepsilon_3}{\varepsilon_2 + \varepsilon_3}} = n_1 \sin \theta_{sp}$$
 (13)

The second term represents the effective RI arising from the interaction between the metal film and the analyte, as illustrated by the solid black line in Fig. 3, where ε_2 and ε_3 denote the dielectric constants of the metal and analyte, respectively. To examine how the waveguide material affects the results, we keep silver constant as the metal material while setting the RI of the analyte (n_3) 1.35.

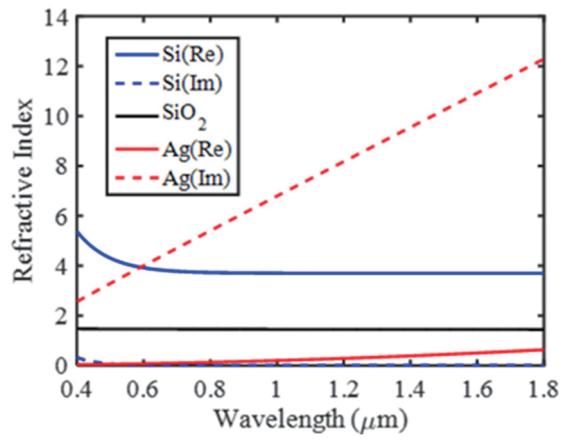


Fig.2. Material dispersions of Silicon, silica, and silver for the visible and near-infrared spectral range.

The third term in eq.(13) corresponds to the effective RI of the waveguide mode, determined by the RI of the waveguide material (n_1) and the angle of incidence (θ_{sp}). Fig. 3 reports the analysis based on the calculated effective RI for a simple structure based on two waveguides, Si and SiO₂, covered by a thin silver layer (40 nm) and the analyte, $n_3 = 1.35$. The solid blue line represents the RI of silicon, while the dashed blue line represents the potential angles of incidence corresponding to the modes that may exist within the waveguide. The angle spans from the critical angle to 90 degrees. Due to the significant difference in RIs between silicon and silica, the critical angle (25.8 degrees) of silicon waveguides is relatively small compared with that of silica (76.8 degrees). Consequently, the computed range between the solid and dashed blue lines varies about 2.93, from 5.24 to 2.31 at wavelength 0.4 µm. Similarly, the solid red line

and the dashed line represent the RI of the silica waveguide and the potential effective RI, respectively. However, due to the small RIs difference between the silica waveguide and the substrate material, set at 0.004 in this study, the critical angle is approximately 76.8 degrees. As a result, the solid and dashed red lines are close, and the calculated range between them only varies by 0.06, ranging from 1.47 to 1.41 at a wavelength of 0.4 μm .

The solid black line shown in Fig. 3 represents the effective RI calculated with the analyte and the silver film. It can be observed that the black line does not intersect with the blue line of the silicon waveguide, indicating that there are no available wavelengths to excite SPP. An analogous situation is found in the analytes are replaced by others with n_3 from 1.36 to 1.55. Although the adjustable range represented by the solid red line and dashed red line denoting the silica waveguide is relatively small, they can intersect with the black line at a wavelength of approximately 0.6 µm, resulting in the generation of SPR. Compared to silicon, the optical properties of silica are more suitable for designing SPR sensors.

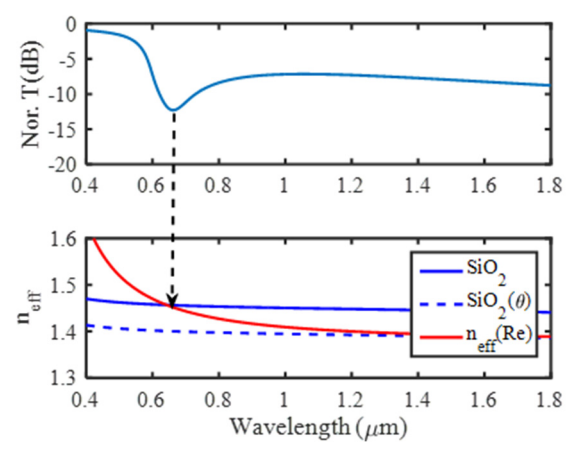


Fig.3. Effective RIs for two waveguides, Si and SiO₂, covered with a thin silver layer (40 nm) and the analytes n₃ of 1.35

3.3 SPR condition

To align with CMOS processes and simplify simulations, a silica planar waveguide with dimensions of 50 µm in length and 0.22 µm in thickness was employed. A 40 nm thick silver film was deposited above the waveguide, and on top of it was an analyte with an RI of 1.35. The incident angle and wavelength determine the occurrence of SPR. According to the theory

discussed in Section 2.3, the N times reflectance $(R_p^{N_{ref}(\theta)})$ within the device can be computed as a function of incident angle and wavelength, as shown in Fig. 4. A decrease in reflection implies energy penetration into the metallic layer above the waveguide, giving rise to the SPR phenomenon. Observing several incident angles, namely the critical angle at 78.6 degrees, along with 80, 85, and 89 degrees, the corresponding SPR wavelengths are $0.600 \mu m$, $0.574 \mu m$, 0.523μm, and 0.510 μm, respectively. Notably, angles above 86 degrees, approaching horizontal incidence (fundamental mode), exhibit distinct resonance wavelengths with high recognition. For angles below 82 degrees, all wavelengths beyond 0.5 µm experience low reflection, resulting in limited resonance identification. Consequently, for waveguide design, a singlemode waveguide is preferable.

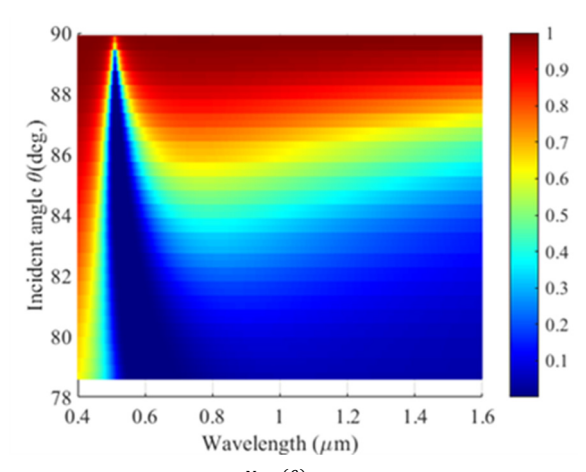


Fig.4. Reflectance $(R_p^{N_{ref}(\theta)})$ at the output of the SPR waveguide as a function of incident angle and wavelength

According to eq. (7), for each wavelength, the cumulative effect of all incident angles at the output end is required to accurately compute the complete normalized transmitted power spectrum, as depicted in Fig. 5.

In Fig. 5(a), it can be observed that SPR exhibits a dip at the wavelength of 0.526 μm, corresponding to a normalized transmitted power of -15.57 dB. At the same wavelength, as illustrated, it coincides precisely with the intersection of the effective RI (solid red line) and the RI of the waveguide (solid blue line). This indicates that the incident angle of p-polarized light is approximately close to 90 degrees for SPR. In Fig. 5(b), as n₃ of the analyte increases to 1.38, the SPR wavelength shifts towards a longer wavelength to 0.662 μm, corresponding to an

effective RI of 1.452. Utilizing the RI associated with silica's dispersion characteristics (1.456), it can be inferred that the primary incident angle of the waveguide when SPR occurs is approximately 85.75 degrees. As the RI of the analyte increases, the SPR wavelength shifts to longer, consistent with numerous literature results[40-42], including our previous work [43]. Changes in the RI of the analyte have an impact on the effective RI and alter the resonance wavelength of SPR.

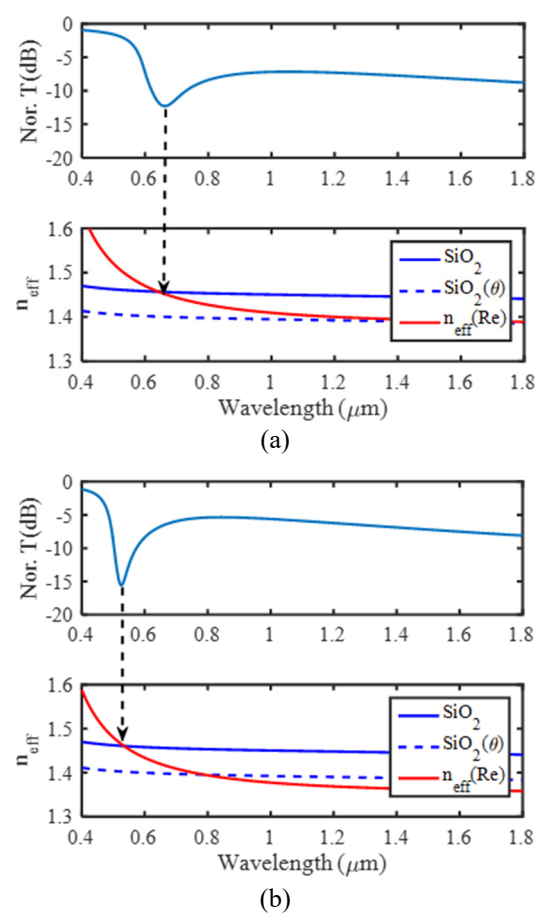


Fig.5. The relationship between SPR spectra and effective RI for (a) n3=1.35, (b) n3=1.38

3.4 Thickness of metal layer (d_2)

The thickness of the metal layer is a crucial parameter for designing an SPR sensor. Under the condition that the n_3 remains at 1.35 and sensing length 50 μ m, the impact of varying the silver film thickness (d_2) from 2 nm to 100 nm, along with wavelengths ranging from 0.4 μ m to 1.6 μ m, on the normalized transmitted power in dB is shown in Fig. 6. Using the threshold of transmitted power below -10 dB as a criterion for optimal SPR design, it is evident from this

spectrum that the favorable range for the metal film thickness lies approximately between 20 nm and 60 nm. Correspondingly, the SPR wavelength shifts from 0.4 μm to about 0.6 μm. As the silver film thickness increases, the shift of the SPR spectrum toward longer wavelengths at the increasing rate of about 4.6. Thicker metal films necessitate longer SPR wavelengths. generation of SPR relies on the excitation of evanescent waves at the boundary when the waveguide propagation mode is passing. These evanescent waves must be able to penetrate the metal film thickness to interact effectively with the analyte. Therefore, the metal film should not be too thick. Conversely, a sufficient metal thickness is also required for metal ion polarization and resonance. Hence, to achieve optimal SPR performance, the selection of metal film thickness must be confined to a specific range, namely 20 nm to 60 nm according to theoretical calculation. From this perspective, SPR has a significant advantage as its spectral position can be finely adjusted by simply changing the thickness of the metal film.

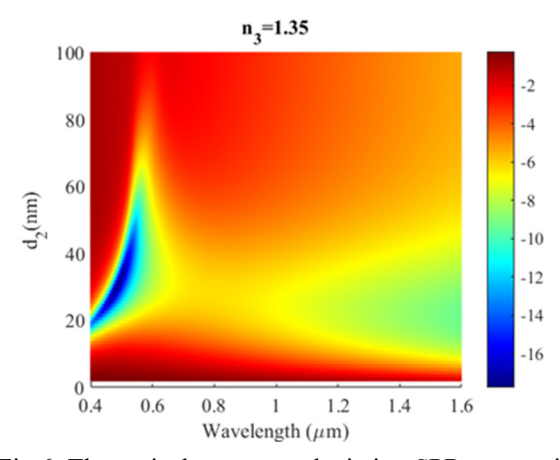


Fig. 6. Theoretical outcomes depicting SPR spectra in relation to variations in metal film thicknesses d_2

3.5 Sensing length (L)

Figure 7 is a plot of the normalized transmitted power (Nor. T.) calculated with sensing lengths (L) of 25 µm, 50 µm,100µm, and 200 µm. As the sensing length increases, the normalized transmitted power exhibits deeper dips. This phenomenon arises from the fact that with increasing L, the number of back-and-forth reflections (N_{ref}) in the waveguide increases. Each reflection excites SPR, and the energy is transferred from the evanescent wave to the

metallic layer above the waveguide, resulting in lower reflectance. A decreasing rate of 0.189 dB/µm in the normalized transmitted power is observed in the range between 25 μm and 50 μm. So, sensing length has a direct impact on the reflection number and therefore has a similar big effect on SPR spectra. Considering a more favorable SPR performance (exceeding -10 dB), the choice of sensing length should be at least greater than 25 µm. However, an excessively long sensing region results in oversized device dimensions, making it challenging to integrate with other CMOS components. For general purposes, a recommendation of 50 µm is suggested. This dimension aligns well with that of microfluidic channels to facilitate future integration into biomedical sensing platforms.

Another observation from Fig. 7 is that the spectra can be roughly divided into a short wavelength SPR region for wavelengths less than 0.6 µm and a decay region for wavelengths greater than 0.8 µm. In the decay region, the normalized transmitted power decreases with increasing wavelength. This phenomenon is attributed to the increase in the imaginary part of the RI of the silver with longer wavelengths, as depicted in Fig. 2.

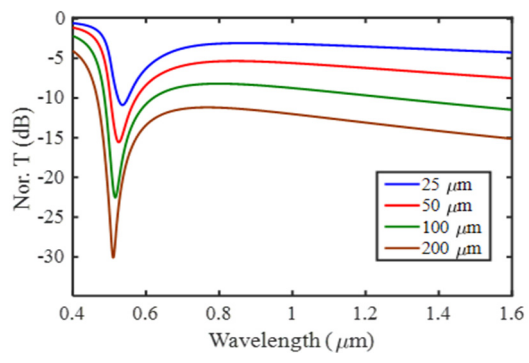


Fig.7. SPR spectra for sensing lengths of 25 μ m, 50 μ m, 100 μ m, and 200 μ m

3.6 Sensitivity

Using the optimized sensor parameters, including a silver film thickness of 40 nm and a sensing length of 50 μ m, spectral calculations were performed for n_3 ranging from 1.3 to 1.5, as shown in Fig. 8. It is evident that as n_3 increases, the corresponding SPR wavelength gradually increases. The sensor is capable of detecting RIs within the range of 1.30 to 1.40. Sensitivity calculations for the SPR sensor can be conducted within this specified range.

Sensitivity, an important characteristic of a

sensor, is defined as the ratio of SPR wavelength change to RI change [44]. Based on Fig. 8, we extracted RIs of the analyte ranging from 1.30 to 1.40 with an interval of 0.02, along with their corresponding SPR wavelengths and normalized transmitted power, as shown in Fig. 9(a) and 9(b). A quadratic fitting function was applied to the six points in Fig. 9(a), resulting in an R^2 value of 0.995. Eq.(14) is the result obtained by deriving the derivative function of the approximation equation, $y = 40.27x^2 - 104.8x + 68.62$, in Fig 9(a). The theoretical results indicate that the SPR sensor exhibits higher sensitivity when detecting analytes with higher RIs. For n_3 of 1.40, the sensitivity can reach up to 7.956 μ m/RIU.

$$S_n(n_3) \equiv \frac{\delta \lambda_{res}}{\delta n} = 80.54 \cdot n_3 - 104.8$$
 (14)

A comparison of SPR sesnors is list in Table 1. Compared to an optical fiber-based SPR sensor, a concave-shaped RI sensor based on localized surface plasmon resonance (LSPR) has been reported as 4.471 µm/RIU [45]. Enhanced sensitivity is achieved with a gold (Au) film and gold nanowires (AuNWs) when dealing with analytes whose refractive index (RI) ranges from 1.33 to 1.38. In comparison, a conventional gold film yields a sensitivity of 0.809 µm/RIU for the identical analyte range. [45]. Moreover, an additional SPR sensor, utilizing a coreless fiber and featuring a shorter length of 1 cm, has been developed. In the RI range of 1.33–1.40, this SPR sensor exhibits wavelength shift a approximately 200 nm towards longer wavelengths. The average refractive sensitivity is determined to be 2.836 µm/RIU, with the highest sensitivity reaching 4.328 µm/RIU [46]. In the case of silicon carbide (SiC) waveguide structure, the SPR optical sensor with an Ag-Au bilayer metal configuration was demonstrated for a sensitivity of 2.581 µm/RIU from a RI range of 1.34 - 1.36 [47]. In addition, we conducted theoretical studies on a pair of highly sensitive SPR sensors using copper (Cu) and aluminum (Al) as surface plasmon excitation layers in the infrared region. The sensitivities of the optimized probes, incorporating field-enhancing graphene and silicon layers for Cu and Al, respectively, were found to be exceptionally high at 23.50 and 24 µm/RIU [48]. In comparison to other SPR sensors, our sensitivity surpasses that of the majority. It's noteworthy to mention that the silica-based SPR structure proposed in this study stands out for its simplicity and robustness,

utilizing low-cost materials and offering ease of mass production. Importantly, this design facilitates subsequent surface modification processes for biosensors.

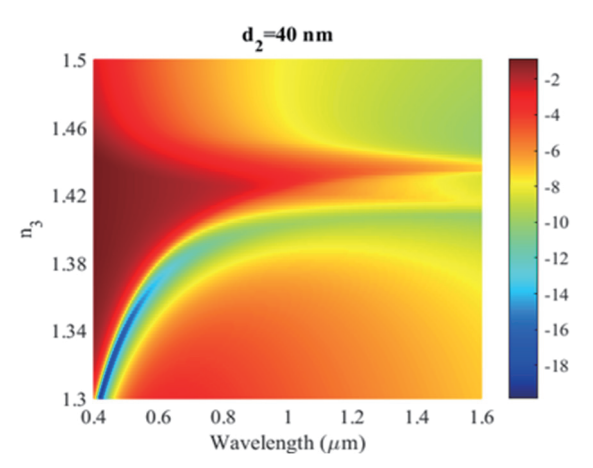


Fig.8. SPR Spectra for the silver thicknesses of 40 nm

Quadratic: $y = 40.27*x^2 - 104.8*x + 68.62$

 $R^2 = 0.995$

0.9

0.8

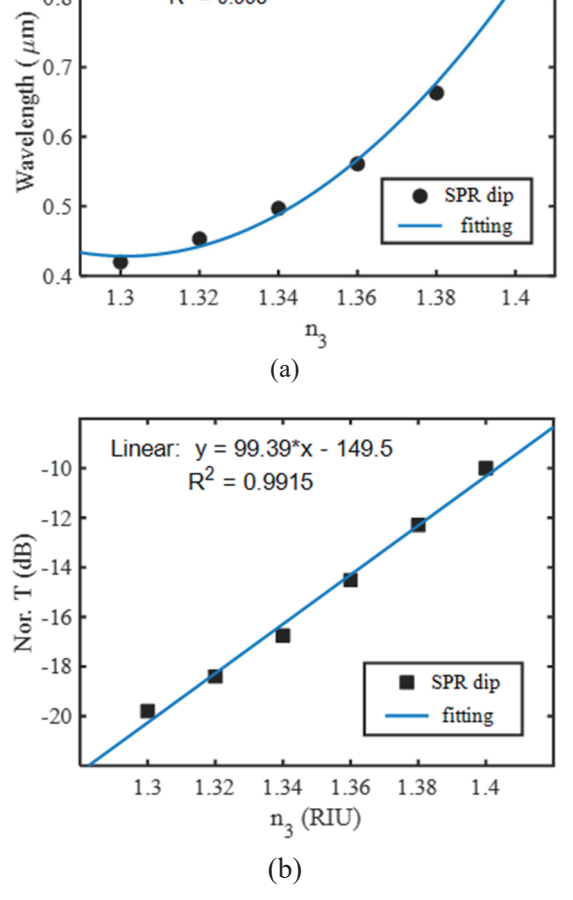


Fig.9. (a) SPR wavelengths and (b) normalized transmitted power corresponding to the analyte RIs

Table 1. Comparison of SPR sesnors

structure	film	analyte	Sn	Ref.
LSPR Fiber	Au-NW	1.33-1.38	4.471	[45]
Coreless fiber	Au	1.33-1.40	4.328	[46]
SiC on SiO ₂	Ag+Au	1.33-1.36	2.581	[47]
Si-GP-Metal- fiber	Cu, Al	1.33-1.332	23.50, 24.0	[48]
SiO2	Ag	1.30-1.40	7.956	this

NW: narrow wire; GP: graphene

IV. CONCLUSIONS

The design of an SPR sensor on silicon photonics is proposed and simulated theoretically. Leveraging material dispersion characteristics, we discuss the relationship between the excitation conditions of SPR and the choice of waveguide materials from the perspective of effective RI. Our analysis reveals that silica is the optimal waveguide material rather than silicon for SPR devices. Regarding SPR sensor dimensions, we not only opted for a waveguide thickness of 0.22 um, which aligns with CMOS fabrication processes but also conducted theoretical calculations to determine the optimal range for the metal film thickness. The preferred silver film thickness falls within the range of 20 nm to 60 nm, and correspondingly, the SPR wavelength increases from 0.4 µm to 0.6 µm. Thicker films result in longer SPR wavelengths. Within this thickness range, the SPR wavelength increasing rate is 4.6. Besides, the sensing length should be greater than 25 µm. A decreasing rate of 0.189 dB/µm in the normalized transmitted power is observed in the range between 25 μm and 50 μm. Furthermore, the sensitivity was conducted based on these optimized parameters. This analysis resulted in a sensitivity function correlated with the RI of the analyte. The theoretical maximum sensitivity of 7.956 μ m/RIU is obtained.

REFERENCES

- [1] S. Y. Siew *et al.*, "Review of silicon photonics technology and platform development," *Journal of Lightwave Technology*, Vol. 39, No. 13, pp. 4374-4389, 2021.
- [2] W. Bogaerts and L. Chrostowski, "Silicon photonics circuit design: methods, tools and challenges," *Laser & Photonics*

- Reviews, Vol. 12, No. 4, pp. 1700237, 2018.
- [3] W. Daniyal, S. Saleviter, and Y. W. Fen, "Development of surface plasmon resonance spectroscopy for metal ion detection," *Sensors and Materials*, Vol. 30, No. 9, pp. 2023-2038, 2018.
- [4] C. Martín-Sánchez, G. González-Rubio, P. Mulvaney, A. Guerrero-Martínez, L. M. Liz-Marzán, and F. Rodríguez, "Monodisperse Gold Nanorods for High-Pressure Refractive Index Sensing," *The journal of physical chemistry letters*, Vol. 10, No. 7, pp. 1587-1593, 2019.
- [5] A. Azzouz *et al.*, "Advances in surface plasmon resonance—based biosensor technologies for cancer biomarker detection," *Biosensors and Bioelectronics*, Vol. 197, pp. 113767, 2022.
- [6] J.-H. Park, Y.-W. Cho, and T.-H. Kim, "Recent advances in surface plasmon resonance sensors for sensitive optical detection of pathogens," *Biosensors*, Vol. 12, No. 3, pp. 180, 2022.
- [7] M. Sobolevskyi *et al.*, "Application of modified gold nanoparticles to improve characteristics of DNA hybridization biosensor based on surface plasmon resonance spectrometry," *Applied Nanoscience*, pp. 1-9, 2023.
- [8] R. C. Jorgenson and S. S. Yee, "A fiber-optic chemical sensor based on surface plasmon resonance," *Sensors and Actuators B: Chemical*, Vol. 12, No. 3, pp. 213-220, 1993.
- [9] K. Sathiyamoorthy, B. Ramya, V. M. Murukeshan, and X. W. Sun, "Modified two prism SPR sensor configurations to improve the sensitivity of measurement," *Sensors and Actuators A: Physical*, Vol. 191, pp. 73-77, 2013.
- [10] H. Yang, J. Song, D. Zhang, and Y. Huang, "A symmetrical surface plasmon resonance sensing structure excited by a stripe waveguide," *Optik International Journal for Light and Electron Optics*, Vol. 127, No. 20, pp. 8629-8637, 2016.
- [11] G. Wang, C. Wang, and S. Sun, "An optical waveguide sensor based on mesoporous silica films with a comparison to surface plasmon resonance sensors," *Sensors and Actuators B: Chemical*, Vol. 255, Part 3, pp. 3400-3408, 2018.
- [12] A. Fantoni, J. Costa, M. Fernandes, Y. Vygranenko, and M. Vieira, "Theory and

- FDTD simulations of an amorphous silicon planar waveguide structure suitable to be used as a surface plasmon resonance biosensor," *Optica Pura y Aplicada*, Vol. 53, No. 2, pp. 1-8, 2020.
- [13] A. S. Hasan, R. J. Al-Azawi, and A. A. Alwahib, "Theory and modeling of slab waveguide based surface plasmon resonance," *Engineering and Technology Journal*, Vol. 40, No. 08, pp. 1082-1089, 2022.
- [14] H. Fu *et al.*, "A high sensitivity D-type surface plasmon resonance optical fiber refractive index sensor with graphene coated silver nano-columns," *Optical fiber technology*, Vol. 48, pp. 34-39, 2019.
- [15] T. Cheng *et al.*, "A surface plasmon resonance optical fiber sensor for simultaneous measurement of relative humidity and temperature," *IEEE Sensors Journal*, Vol. 22, No. 4, pp. 3246-3253, 2022.
- [16]R. A. Kadhim, A. K. K. Abdul, and L. Yuan, "Advances in surface plasmon resonance-based plastic optical fiber sensors," *IETE Technical Review*, Vol. 39, No. 2, pp. 442-459, 2022.
- [17] A. Philip and A. R. Kumar, "The performance enhancement of surface plasmon resonance optical sensors using nanomaterials: A review," *Coordination Chemistry Reviews*, Vol. 458, pp. 214424, 2022.
- [18] Q. Wang *et al.*, "Research advances on surface plasmon resonance biosensors," *Nanoscale,* Vol. 14, No. 3, pp. 564-591, 2022.
- [19] G. S. Mei, P. S. Menon, and G. Hegde, "ZnO for performance enhancement of surface plasmon resonance biosensor: a review," *Materials Research Express*, Vol. 7, No. 1, pp. 012003, 2020.
- [20] E. Luan, H. Shoman, D. M. Ratner, K. C. Cheung, and L. Chrostowski, "Silicon Photonic Biosensors Using Label-Free Detection," *Sensors-Basel*, Vol. 18, No. 10, pp. 3519, 2018.
- [21] A. Fernández Gavela, D. Grajales García, J. C. Ramirez, and L. M. Lechuga, "Last Advances in Silicon-Based Optical Biosensors," *Sensors-Basel*, Vol. 16, No. 3, pp. 285, 2016.
- [22] L. Jin, C. Bao-xue, Y. Hai-ma, and M. Iso, "Symmetric surface plasmon resonance

- sensing structure excited by a planar waveguide," *Optics & Laser Technology*, Vol. 44, No. 7, pp. 2286-2291, 2012.
- [23] S. Nayak, N. R. Blumenfeld, T. Laksanasopin, and S. K. Sia, "Point-of-Care Diagnostics: Recent Developments in a Connected Age," *Analytical Chemistry*, Vol. 89, No. 1, pp. 102-123, 2017.
- [24] H. Shafiee *et al.*, "Paper and Flexible Substrates as Materials for Biosensing Platforms to Detect Multiple Biotargets," *Scientific Reports*, Vol. 5, No. 1, pp. 8719, 2015.
- [25] S. Wu, X. Mu, L. Cheng, S. Mao, and H. Fu, "State-of-the-art and perspectives on silicon waveguide crossings: A review," *Micromachines*, Vol. 11, No. 3, pp. 326, 2020.
- [26] Y. Su, Y. Zhang, C. Qiu, X. Guo, and L. Sun, "Silicon photonic platform for passive waveguide devices: Materials, fabrication, and applications," *Advanced Materials Technologies*, Vol. 5, No. 8, pp. 1901153, 2020.
- [27] N. A. S. Omar *et al.*, "Experimental evaluation on surface plasmon resonance sensor performance based on sensitive hyperbranched polymer nanocomposite thin films," *Sensors and Actuators A: Physical*, Vol. 303, pp. 111830, 2020.
- [28] Y. Zhao, S. Gan, G. Zhang, and X. Dai, "High sensitivity refractive index sensor based on surface plasmon resonance with topological insulator," *Results in Physics*, Vol. 14, pp. 102477, 2019.
- [29] I. R. Matias, I. Del Villar, and J. M. Corres, "Lossy mode resonance based sensors in planar configuration: a review," *IEEE Sensors Journal*, 2023.
- [30] I. Vitoria, C. Ruiz Zamarreño, A. Ozcariz, and I. R. Matias, "Fiber Optic Gas Sensors Based on Lossy Mode Resonances and Sensing Materials Used Therefor: A Comprehensive Review," *Sensors*, Vol. 21, No. 3, pp. 731, 2021.
- [31] T. Feuchter, E. K. Mwarania, J. Wang, L. Reekie, and J. S. Wilkinson, "Erbium-doped ion-exchanged waveguide lasers in BK-7 glass," *Ieee Photonic Tech L*, Vol. 4, No. 6, pp. 542-544, 1992.
- [32] A. Tervonen, B. R. West, and S. Honkanen, "Ion-exchanged glass waveguide technology: a review," *Optical Engineering*, Vol. 50, No. 7, pp. 071107-15,

- 2011.
- [33] Y. Kim, D. Kim, and D. Yoon, "PECVD SiO2 and SiON films dependant on the rf bias power for low-loss silica waveguide," *Thin Solid Films,* Vol. 475, No. 1-2, pp. 271-274, 2005.
- [34] Q. Lai, J. Gu, M. Smit, J. Schmid, and H. Melchior, "Simple technologies for fabrication of low-loss silica waveguides," *Electronics Letters*, Vol. 28, No. 11, pp. 1000-1001, 1992.
- [35] N. Paliwal and J. John, "Lossy Mode Resonance Based Fiber Optic Sensors," in Fiber Optic Sensors: Current Status and Future Possibilities, I. R. Matias, S. Ikezawa, and J. Corres, Eds. Cham: Springer International Publishing, pp. 31-50, 2017.
- [36] D. E. Aspnes and A. Studna, "Dielectric functions and optical parameters of si, ge, gap, gaas, gasb, inp, inas, and insb from 1.5 to 6.0 ev," *Physical review B*, Vol. 27, No. 2, pp. 985, 1983.
- [37] K. Shah, N. K. Sharma, and V. Sajal, "SPR based fiber optic sensor with bi layers of indium tin oxide and platinum: A theoretical evaluation," *Optik International Journal for Light and Electron Optics*, Vol. 135, pp. 50-56, 2017.
- [38] Y. S. Dwivedi, A. K. Sharma, and B. D. Gupta, "Influence of skew rays on the sensitivity and signal-to-noise ratio of a fiber-optic surface-plasmon-resonance sensor: a theoretical study," *Appl. Opt.*, Vol. 46, No. 21, pp. 4563-4569, 2007.
- [39] S. K. Srivastava, R. Verma, and B. D. Gupta, "Theoretical modeling of a self-referenced dual mode SPR sensor utilizing indium tin oxide film," *Optics Communications*, Vol. 369, pp. 131-137, 2016.
- [40] Y. Chen and H. Ming, "Review of surface plasmon resonance and localized surface plasmon resonance sensor," *Photonic Sensors*, Vol. 2, No. 1, pp. 37-49, 2012.
- [41] V. Yesudasu, H. S. Pradhan, and R. J. Pandya, "Recent progress in surface plasmon resonance based sensors: A comprehensive review," *Heliyon*, Vol. 7, No. 3, 2021.
- [42] A. Pathak and V. Singh, "Theoretical assessment of D-shaped optical fiber chemical sensor associated with nanoscale silver strip operating in near-infrared

- region," *Optical and Quantum Electronics*, Vol. 52, No. 4, pp. 1-13, 2020.
- [43] Y.-C. Lin, L.-Y. Chen, and F.-C. Chiu, "Lossy Mode Resonance-Based Glucose Sensor with High-κ Dielectric Film," *Crystals*, Vol. 9, No. 9, pp. 450, 2019.
- [44] A. K. Sharma and B. D. Gupta, "On the sensitivity and signal to noise ratio of a step-index fiber optic surface plasmon resonance sensor with bimetallic layers," *Optics Communications*, Vol. 245, No. 1-6, pp. 159-169, 2005.
- [45] A. K. Pathak, B. A. Rahman, V. K. Singh, and S. Kumari, "Sensitivity enhancement of a concave shaped optical fiber refractive index sensor covered with multiple Au nanowires," *Sensors*, Vol. 19, No. 19, pp. 4210, 2019.
- [46] F. Han *et al.*, "Surface plasmon resonance sensor based on coreless fiber for high sensitivity," *Optical Fiber Technology,* Vol. 50, pp. 172-176, 2019.
- [47] W. Du and F. Zhao, "Silicon carbide based surface plasmon resonance waveguide sensor with a bimetallic layer for improved sensitivity," *Materials Letters*, Vol. 186, pp. 224-226, 2017.
- [48] A. K. Mishra, S. K. Mishra, and A. P. Singh, "Giant infrared sensitivity of surface plasmon resonance-based refractive index sensor," *Plasmonics*, Vol. 13, pp. 1183-1190, 2018.